PNAS RESEARCH ARTICLE | EARTH, ATMOSPHERIC, AND PLANETARY SCIENCES OPEN ACCESS

High time-resolved studies of stick–slip show similar dilatancy to fast and slow earthquakes

Wei Hu[a,1], Yi Ge[a,1], Qiang Xu[a], Runqiu Huang[a], Qi Zhao[b], Huaixiao Gou[a], Mauri McSaveney[a,c], Chingshung Chang[d], Yan Li[a], Xiaoping Jia[e], and Yujie Wang[a,f]

Edited by David Weitz, Harvard University, Cambridge, MA; received March 29, 2023; accepted October 7, 2023

Fast and slow earthquakes are two modes of energy release by the slip in tectonic fault rupture. Although fast and slow slips were observed in the laboratory stick–slip experiments, due to the sampling rate limitation, the details of the fault thickness variation were poorly understood. Especially, why a single fault would show different modes of slip remains elusive. Herein, we report on ring shear experiments with an ultrahigh sampling rate (10 MHz) that illuminate the different physical processes between fast and slow slip events. We show that the duration of slips ranged from dozens to hundreds of milliseconds. Fast slip events are characterized by continuous large-amplitude AE (acoustic emission) and somewhat intricate variation of the sample thickness: A short compaction pulse during the rapid release of stress is followed by dilation and vibrations of the sample thickness. As the slip ends, the thickness of the sample first recovers by slow compaction and then dilates again before nucleation of the following slip event. In contrast, during slow slip events, the shear stress reduction is accompanied by intermittent bursts of low-amplitude AE and sample dilation. We observed the detailed thickness variation during slips and found that dilation occurs during both fast and slow slips, which is consistent with natural observations of coseismic dilatation. This study may be used to reveal the mechanism of fault slips during fast and slow earthquakes, which explain the potential effect of fast and slow slips on stress redistribution and structural rearrangement in faults.

fast and slow earthquake | coseismic dilation | stick–slip | acoustic emission | granular materials

Significance

The faults slip abruptly to cause catastrophic fast earthquakes, while slow earthquakes gently release energy. Understanding the slip process in the granular assemblies is important for revealing the slip mechanism of real fault. Different from previous laboratory observations of only dilation or compaction in the fast slips, we first found the detailed variation of granular fault thickness at ultrahigh temporal resolution: Compaction occurred first, then accompanied by dilation and vibration, and finally slow compaction initiated after cessation of the fast slip. We also observed the dilation of slow slip in the laboratory. These dilation events of fast and slow slips were also observed in natural earthquakes, which have implications for understanding mechanisms underlying fault slip instabilities.

Fast earthquakes and slow earthquakes are two modes of tectonic fault slip with different energy release durations (1). Fast earthquakes are often accompanied by catastrophic ground motion, causing a serious disaster (2, 3). While fast earthquakes are conventional fast tectonic fault earthquakes with catastrophic slip failure (1, 3), earthquakes with slow slip failure that last several hours to months have also been observed in the field, such as low-frequency earthquakes and slow slip earthquakes (4–8). Although slow earthquakes do not cause catastrophic ground motion, their process of slow stress release may play roles in stress transfer and stress redistribution in faults, potentially triggering fast earthquakes (8–11). Fast earthquakes and slow earthquakes have been frequently observed in situ, but field seismic studies are difficult to carry out. Fault stick–slip is a possible significant mechanism for earthquakes (2). Many laboratory earthquake simulations have studied the mechanism of fast and slow slip events with physical stick–slip experiments (3, 12–17) and numerical simulations (1, 18, 19). Recent observations suggest that fast and slow slip modes were mainly controlled by the interplay of fault frictional properties, effective normal stress, and the elastic stiffness of the surrounding material (16). The velocity dependence of the frictional rate parameter and critical slip distance also play an important role in the mode of slip (17). However, why fast earthquakes and slow earthquakes would occur in the same fault is still difficult to understand (1). Fast and slow earthquakes may obey different scaling laws, and this scaling behavior demonstrates that fast and slow earthquakes can be thought of as different manifestations of the same fault motion phenomena (20), which would indicate that these slow earthquakes are governed by fundamentally different mechanisms than fast earthquakes (17). The stick–slip experiments of granular materials have been carried out (13–17), there has never been a synchronous ultrahigh speed acquisition experiment. Due to sampling rate limitations, it is difficult to capture the high-resolution granular fault thickness variation process of fast-slip and slow-slip events and analyze their detailed physical mechanisms. In previous laboratory studies, it was observed that granular fault compacts during fast-slip events and dilates during the stick process (13, 21–24). Instead, the granular fault dilates during the fast-slip events were observed by one laboratory experiment (25) and molecular dynamics simulations (26, 27). It is still a puzzle about whether the sample thickness is dilated or

Author contributions: W.H., Q.X., Q.Z., H.G., M.M., C.C., Y.L., X.J., and Y.W. designed research; W.H., Y.G., Q.X., Q.Z., H.G., C.C., Y.L., X.J., and Y.W. performed research; W.H. and Y.G. contributed new reagents/analytic tools; W.H. and R.H. analyzed data; and W.H. and Y.G. wrote the paper.

The authors declare no competing interest.

This article is a PNAS Direct Submission.

[1]To whom correspondence may be addressed. Email: huwei1999@126.com or 1479856303@qq.com.

This article contains supporting information online at https://www.pnas.org/lookup/suppl/doi:10.1073/pnas.2305134120/-/DCSupplemental.

Published November 15, 2023.

compacted during the fast slips (22, 25), and there is basically no conclusion on the mechanism of slow slips. A general physical mechanism of fast and slow slip modes remains enigmatic (4–6). Stress changes due to the earthquake slip, both dynamic and static, have long been thought to cause dilatancy in the fault zone that recovers (compaction) after the earthquake (28–30). The dilation of the fault zone during co-seismic slip in the 2019 Ridgecrest earthquakes has been directly observed by analyzing co-seismic strain tensors (28). Previously, this type of dilatancy had only been inferred through post-seismic analysis (29, 30). High temporal resolution is critical for capturing the coseismic slip rupture of faults. Moreover, in laboratory experiments, it is necessary to use a high temporal resolution acquisition system to monitor the stick–slip dynamic process, which may provide insight into the dynamic slip mechanism of earthquakes.

The concept of force chains has been used in explanations of the mechanical properties of granular materials (31–34). Fault gouge is composed of granular packings (13, 16, 23, 24), and the stick–slip of granular packings is related to the formation and destruction of force chain. Under the shear load, the granular assemblies are anisotropic (34), and the force chain is not uniform in space, forming force chains with different strengths (35–38). The failure modes of different force chain networks may control the stick–slip behavior of granular assemblies. In stick–slip instability, force chain buckling and reforming are associated with the shearing of the granular assemblies, which correspond to the storage and release of elastic strain energy (35, 37). In the sheared granular assemblies, the collisions of grains cause abrupt perturbation of the force chain and release elastic strain energy (32, 33). The released energy typically leads to the generation of elastic waves in the kHz frequency range (39), termed acoustic emission (AE). AE is now commonly used to indirectly detect microphysical events during the stick–slip behavior of granular assemblies (39–41). These AE events carry spectral information on physical behavior during shearing. Some studies suggest that the burst of AEs may be generated by the collision between grains (39, 40, 42). The relationship between AEs and different slip modes is rarely noticed (24). Due to the lack of synchronous ultrahigh sampling rate acquisition for shear stress (SS), AE, and sample thickness variation during stick–slip, the mechanism of fast and slow slip events is still unclear. Meanwhile, the low-resolution time sequence results could not explain the detailed granular fault thickness variation and physical scenarios during slips.

Here, we used a synchronous ultrahigh speed (10 MHz sampling rate) acquisition system to record SS, AE, and sample thickness variation during stick–slip in a ring shear apparatus. We carried out statistical analysis of these slip event types and refined analysis of AEs, SS, and sample thickness synchronously. These are discussed in the context of the physical mechanisms and slip failure processes. Moreover, the synchronous ultrahigh speed acquisition system allows us to directly measure phenomena such as the precise thickness variation process that previously were only observed as compaction (13, 21–24) or dilation (25) at low temporal resolution (seconds time scale) during fast slip. The sampling rate in these studies ranges from 1 kHz to 1 MHz. Nevertheless, there is rarely synchronous time series analysis of SS drop and sample thickness variation with high time resolution (millisecond time scale). Fast slip events are characterized by somewhat intricate variation of the sample thickness: A short compaction pulse during the rapid release of stress is followed by dilation and vibrations of the sample's thickness. Using accurate displacement monitoring, we observed dilation during the slow-slip event. These fast and slow slip events with the dilation process have similar dilatancy characteristics to natural fault slip events (28–30), which would shed light on the underlying mechanisms of both catastrophic fast earthquakes and slow earthquakes.

Results

Characteristics of Laboratory Stick–Slip Events. Fig. 1*A* depicts the variation of SS in uniform-size (0.8 to 1 mm) glass sphere ring shear tests (*Materials and Methods*), conducted at four different normal stresses (900 kPa, 1100 kPa, 1300 kPa, 1500 kPa), with respect to shear duration. Many drops in SS characterize the curves. Stick–slip events are observed under all four normal stress conditions and show normal-stress dependence. One representative stick–slip cycle with fast-slip and slow-slip events under the condition of 1,500 kPa is illustrated in Fig. 1*B*. Points A and B represent the start and the cessation of the stress drop in the fast-slip event. Points C and D represent the start and the cessation of the stress drop in the slow-slip event.

Three phases of the stick–slip process (Fig. 1*B*) can be recognized in the results: fast slip (phase I A-B), stick (phase II B-C), and slow slip (phase III C-D). A fast and large stress drop (average stress decrease rate of 6,081.45 kPa/s) occurred in phase I, accompanied by a large-amplitude AE (>30 mV) (Fig. 1*C*). At this temporal resolution (8,000 ms), we observe the dilation of the sample thickness in the fast slip process and slow compaction (hundreds of milliseconds) of the sample thickness after the fast stress drop (Fig. 1*D*). After the fast slip (phase I A-B), the stick phase II was initiated (Fig. 1*B*). The stick process corresponded to a gradual increase in SS in the granular assemblies with the accumulation of elastic strain energy. Moreover, in the progression of the stick phase, we observed slow and small releases of SS (average stress decrease rate of 35.61 kPa/s) (Fig. 1*B*) accompanied by intermittent releases of AEs (Fig. 1*C*), defined as the slow slip (phase III C-D), with only a dilation (Fig. 1*D*) during this process. Then, the granular assemblies enter the next stick phase, continuing to accumulate elastic strain energy until the next slip event occurs (Fig. 1*B*).

We plot the fast-slip event (A-B) and slow-slip event (C-D) in Fig. 1*B* into the same time window (600 ms) and compare the difference between the two modes of slip events (Fig. 1 *E* and *H*). It can be observed that the slip duration of the fast-slip event (~15 ms) is shorter than that of the slow-slip event (~300 ms). In the fast-slip event, the granular assemblies release an AE event with a large amplitude (>30 mV) (Fig. 1*F*). During the 600 ms temporal resolution, at the beginning of the stress drop at point A (Fig. 1*E*), the sample thickness experienced dilation followed by vibration (Fig. 1*G*), the vibration persisted after the stress drop ceased at point B (Fig. 1*E*) and continued until the slow compaction of the sample thickness began (Fig. 1*G*). However, at a higher temporal resolution (45 ms), we observed a short compaction pulse (~2 ms) as the stress began to decrease (Fig. 2*C*). In the slow-slip event, we observed that the granular assemblies intermittently release several AEs bursts with smaller amplitudes (<30 mV) (Fig. 1*I*) during slow stress drop (C-D in Fig. 1*H*); we also observed a dilation in the slow-slip process (Fig. 1*J*). Similar mechanical behaviors of the stick–slip cycle were observed under all of the different normal stress conditions (*SI Appendix*, Figs. S1 and S2). However, it should be noted that there were also many slow-slip events during the stick process (*SI Appendix*, Fig. S1). Fast-slip events are usually followed by an alternating sequence of stick and slow-slip intervals.

High Time-Resolved Analysis of the Fast-Slip Event. For high time-resolved analysis of the fast-slip event, we increased the temporal resolution to 45 ms. The fast-slip event sequences of SS, AE waveform, sample height (SH), and AE spectrum in the time domain (45 ms) are shown in Fig. 2. We observed obvious

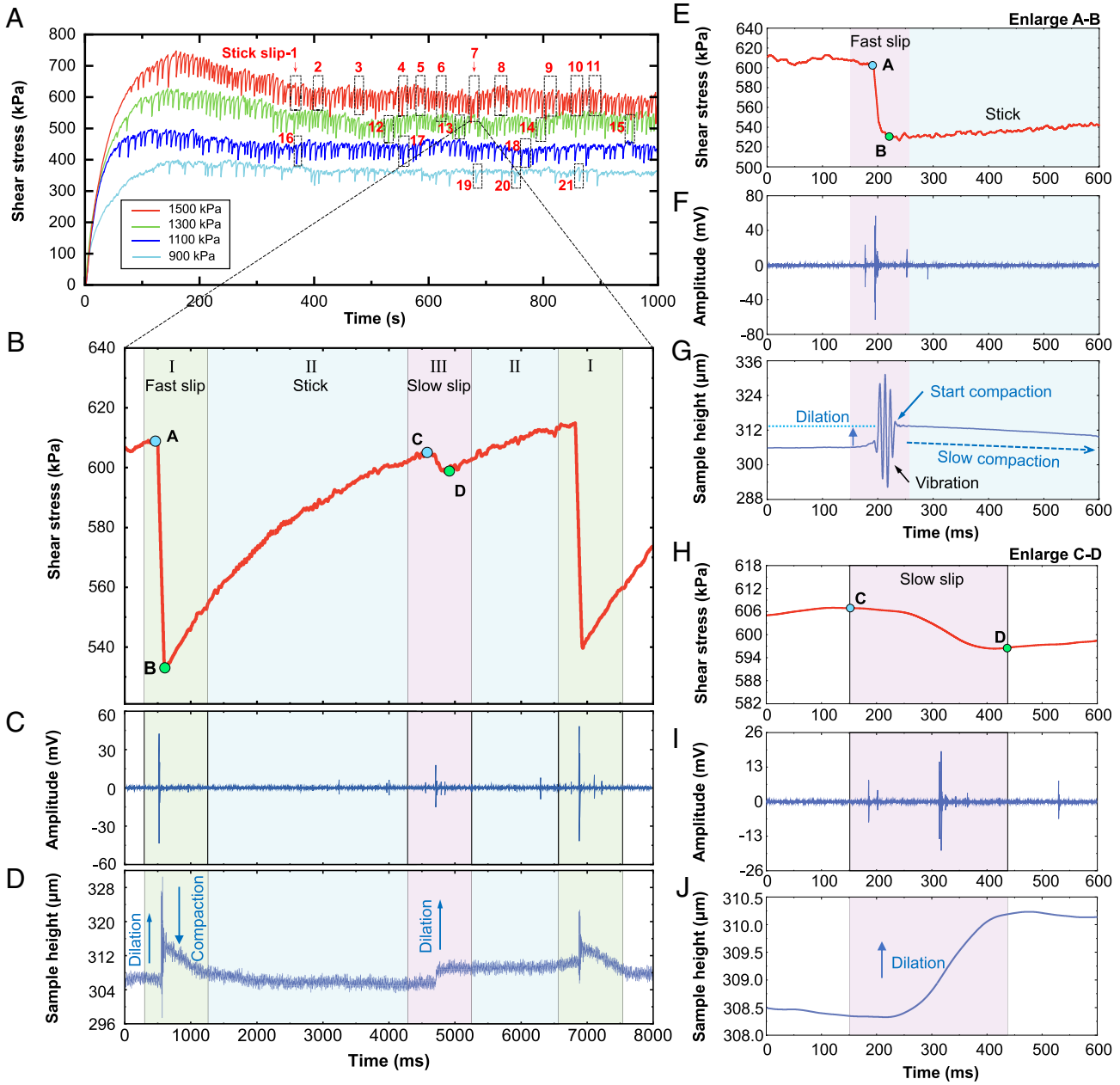

Fig. 1. Measured data in uniform-size glass sphere ring shear experiment with a selected representative stick–slip cycle. (*A*) SS as a function of shear duration. Selection of stick–slip events marked by red numbers. (*B–D*) Detail of simultaneous measurement SS, AE waveform, and SH for two slip events at 1,500 kPa (selected stick slip-7 in Fig. 1*A*). Data reveal three phases during the stick–slip process: fast slip (phase I) from A (start of stress drop in fast slip) to B (cessation of stress drop in fast slip), stick (phase II) from B to C, and slow slip (phase III) from C (start of stress drop in slow slip) to D (cessation of stress drop in slow slip). The color blocks in the figures only roughly indicate the scope of the three phases; the three phases are demarcated by letters A, B, C, and D. Increase in SH upward represents sample thickness dilation. At this temporal resolution (8,000 ms), the dilation of the sample thickness and the slow compaction during the fast-slip event were illustrated in Fig. 1*D*, while only the dilation of the sample thickness was observed during the slow-slip event. (*E–G*) Details of the fast-slip event in Fig. 1*B*, at this temporal resolution (600 ms), the sample thickness dilation, vibration, and slow compaction were observed in Fig. 1*G*. (*H–J*) Details of the slow-slip event in Fig. 1*B*; the red curve is the SS after average smoothing of the purple raw data. The dilation of the sample thickness was observed in Fig. 1*J*.

AEs signals during the time series A-B (Fig. 2 *A* and *B*), which indicates that the granular assemblies slip rapidly during the time series A-B. Thus, the SS decreased from A to B was defined as the total stress drop in the fast-slip event. As shown in Fig. 2*A*, the total stress drop (τ_A-τ_B) across the fast-slip event was 75.41 kPa, and the slip duration (t_B-t_A) was 12.40 ms. A close look reveals a transition point (T point) during stress drop (Fig. 2*A*), which indicates that there are two stress drop processes (A-T and T-B) in the fast-slip event. The fast-slip event started with a large stress drop process (A-T) (average stress decrease rate of 28.14 kPa/ms), which released large SS (63.04 kPa) in a very short time (2.24 ms). When the stress reached the transition point in Fig. 2*A*, we noticed a minor stress drop process (T-B) with an average stress decrease rate of 1.21 kPa/ms. During this process, the SS slightly strengthened and then gradually decreased until reaching point B. This minor stress drop process lasted for 10.16 ms and resulted in a smaller stress drop of 12.37 kPa (Fig. 2*A*). Then, the sheared granular assemblies entered stick phase II, and the elastic strain energy accumulated in the shearing process (Fig. 1*B*).

As shown in Fig. 2 *A* and *C*, there are mainly two stages during the fast slip process: short compaction and dilation–vibration; we captured the SS and SH vibrated around the position of equilibrium

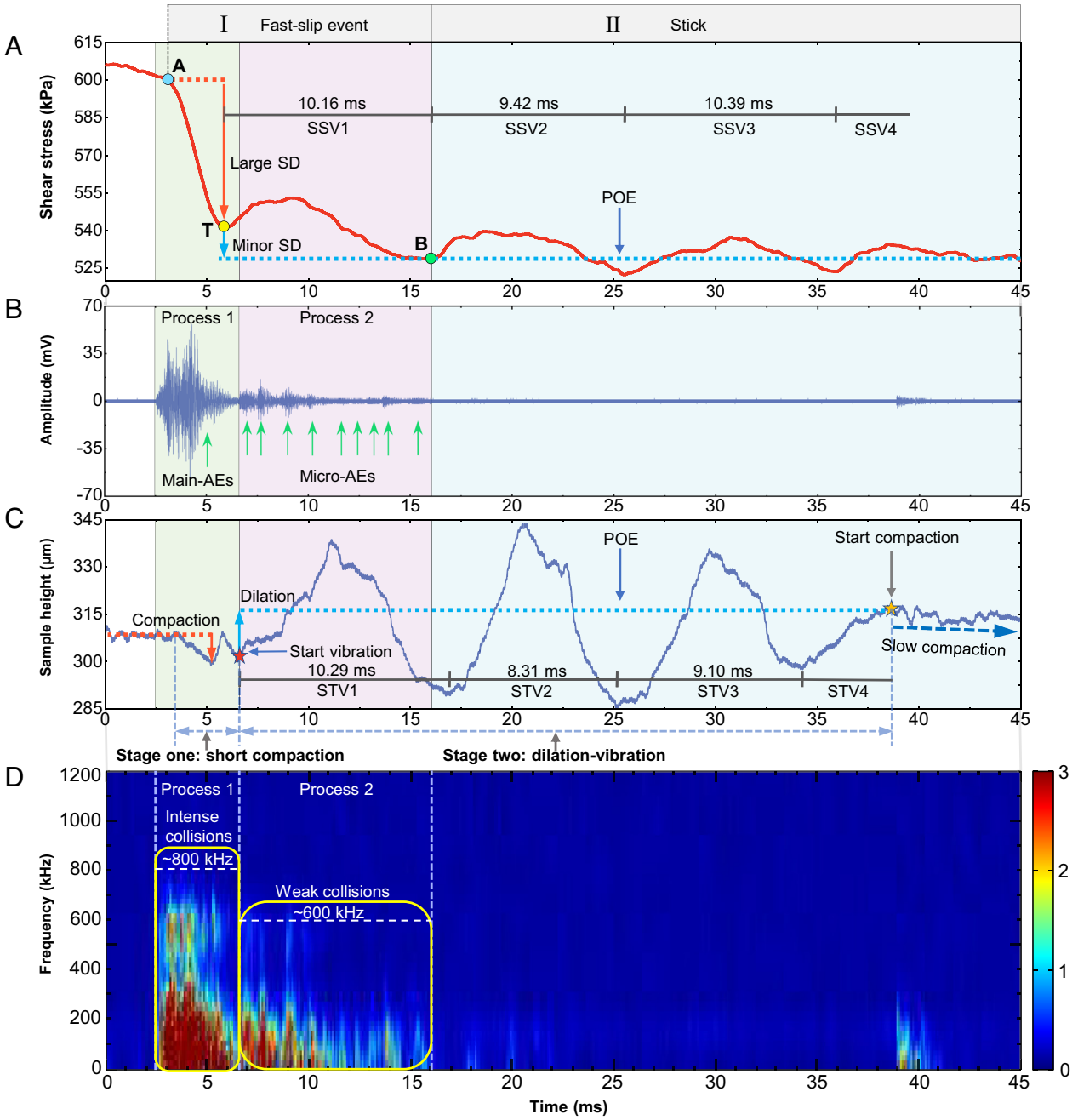

Fig. 2. The selected result of the fast-slip event in Fig. 1*E* depicts the event sequences of SS, AE waveform, SH, and spectrum of AE in the time domain (45 ms). (*A*) Variations in SS with time in 45 ms (Fast slip); the red curve is the SS after smoothing of the raw data. The SS from A to T is released rapidly. The SS from T to B is released slowly while vibrating. The SS enters the stick phase after point B. The red dotted line indicates the SS before stress drop. The blue dotted line indicates the SS after dilation and POE. Large SD is the large stress drop process, minor SD is the minor stress drop process, and SSV is the SS vibration. (*B*) Two processes of AEs excitation in the fast-slip event: process 1 from the start of main-AEs to cessation of main-AEs and process 2 from the cessation of main-AEs to B (cessation of stress drop). Micro-AEs are released in process 2. (*C*) Variations in SH with time in 45 ms; the red pentagon represents the starting of vibration in sample thickness. The red dotted line indicates the SH before compaction. The blue dotted line indicates the SH after dilation and POE. The yellow pentagon represents the starting of slow compaction in sample thickness. STV is the sample thickness vibration. (*D*) The spectrum of AEs in the time domain. In process 1, the frequency bandwidths have high-frequency spectrum (~800 kHz). In process 2, the frequency bandwidths consist of lower frequency AE spectrum (<600 kHz).

(POE) with the help of the ultrahigh speed acquisition system. After the initial large stress drop from A to T, the first SS vibration (SSV1) occurs and gradually releases the minor stress drop. This is followed by SSV2, SSV3, and SSV4 (Fig. 2*A*), we noticed that the vibrations gradually attenuate and come to a stop during SSV4. The distance from the granular assemblies to the unguided LVDT (linear variable differential transformer) sensor is different from that of the torque sensor (*SI Appendix*, Fig. S11*A*), and the elastic wave propagates from the source to the unguided LVDT sensor farther. Thus, we observed a phase difference between the SS vibration and the sample thickness vibration: The onset of the first sample thickness vibration (STV1) lags behind the beginning of the SSV1 (point T in Fig. 2*A*). The thickness of the sample dilates at the start of STV1 (Fig. 2*C*), and subsequently experiences four vibration events: STV1, STV2, STV3, and STV4, we noticed that the vibrations gradually attenuate and come to a stop during STV4. Upon the cessation of the sample thickness vibration, the slow compaction of sample thickness initiates (Figs. 1*G* and 2*C*). Although the vibration of SS is not completely synchronized with the vibration of sample thickness, the average periods of these two kinds of vibrations are 9.99 ms and

9.23 ms, respectively, indicating that the two kinds of vibrations are approximate synchronous vibrations.

The time sequence of the fast-slip event between SS and AE is illustrated in Fig. 2 *A* and *B*. It can be seen that AEs commence prior to the stress drop, which is consistent with previous studies (21). We distinguish two primary categories (Fig. 2*B*) in fast slip progression based on the AEs: process 1 from the start of main-AEs to the cessation of main-AEs and process 2, which follows the cessation of main-AEs to point B (cessation of stress drop). The distinction between the two processes is based on the AE amplitude during fast slip progression. We observed that the maximum AE amplitude (~60 mV) was generated in process 1, and this process was accompanied by compaction of sample thickness (Fig. 2*C*) and large stress drop (Fig. 2*A*). After the main-AE in process 1 is released (Fig. 2*B*), process 2 begins and micro-AEs are observed. However, the amplitudes of these micro-AEs are smaller compared to the main-AEs in process 1. Synchronous acquisition results revealed that the minor stress drop (Fig. 2*A*) and the sample thickness dilation (Fig. 2*C*) occur in process 2, accompanied by the occurrence of SSV1 and STV1.

We employed the short-time Fourier Transform to obtain the AE Time–Frequency spectrum, two distinct groups of AE frequencies in the Time-Frequency spectrum were observed in Fig. 2*D*: the first group consisted of large-amplitude AEs with a high-frequency spectrum of around 800 kHz, which were mainly released during process 1. The second group consisted of small-amplitude AEs with a lower frequency spectrum of less than 600 kHz, which were observed during process 2 (Fig. 2 *B* and *D*). The frequency of the SS vibration and sample thickness vibration was about 100 Hz, far less than the kHz frequency range, indicating that these vibration events occurred in the whole granular assemblies rather than the vibration between grains. Further repeatable synchronous acquisition results of the fast-slip events in 18 ms windows under different normal stresses are illustrated in *SI Appendix*, Figs. S3 and S4.

High Time-Resolved Analysis of Slow-Slip Event. The slow-slip event sequences of SS, AE waveform, SH, and AE spectrum in the time domain (400 ms) are shown in Fig. 3. As shown in Fig. 3*A*, the slow slip process had a small stress drop (τ_C-τ_D 10.17 kPa) and long slip duration (t_D-t_C 285.55 ms). The slow-slip event differed from the fast-slip event, in having no AE signal at the beginning of the stress drop. The high-resolution synchronous analysis of the time sequence shows that the onset of AE lagged behind the slow stress drop (Fig. 3 *A* and *B*), and intermittent AEs burst release was observed in the process of slow stress drop. Moreover, the amplitude of AEs in the slow slip process (Fig. 3*B*) was smaller than that of main-AEs in the fast-slip event (Fig. 2*B*). It should be noted that sample thickness dilation initiated during the stress drop process rather than at the stress drop starting point C (Fig. 3 *A* and *C*). The AE spectrum in the slow slip process was shown in Fig. 3*D*. We zoom into time windows of 5 ms to analyze each AE (AE 1-12) during the slow slip process, and three AE signals were observed: AE-1, AE-3, and AE-4, which show high frequency-spectrum reaching ~600 kHz, while other signals have lower frequencies (<300 kHz) (*SI Appendix*, Fig. S5).

We compared the power spectrum of fast and slow slips quantitatively by plotting the marginal spectrum (amplitude vs. frequency) in a specific time window of 8 ms (Fig. 3*E*). The background noise signal is at the lowest end and can be basically ignored. Main-AEs and micro-AEs were taken from the fast slip event in Fig. 2*B*, and AEs 1-12 were taken from the slow slip event in Fig. 3*B*. These AE signals from fast and slow slips have similar frequency-amplitude profiles, and the dominant frequency is around 110 kHz. The amplitude of the main-AEs is the highest, and the cutoff frequency

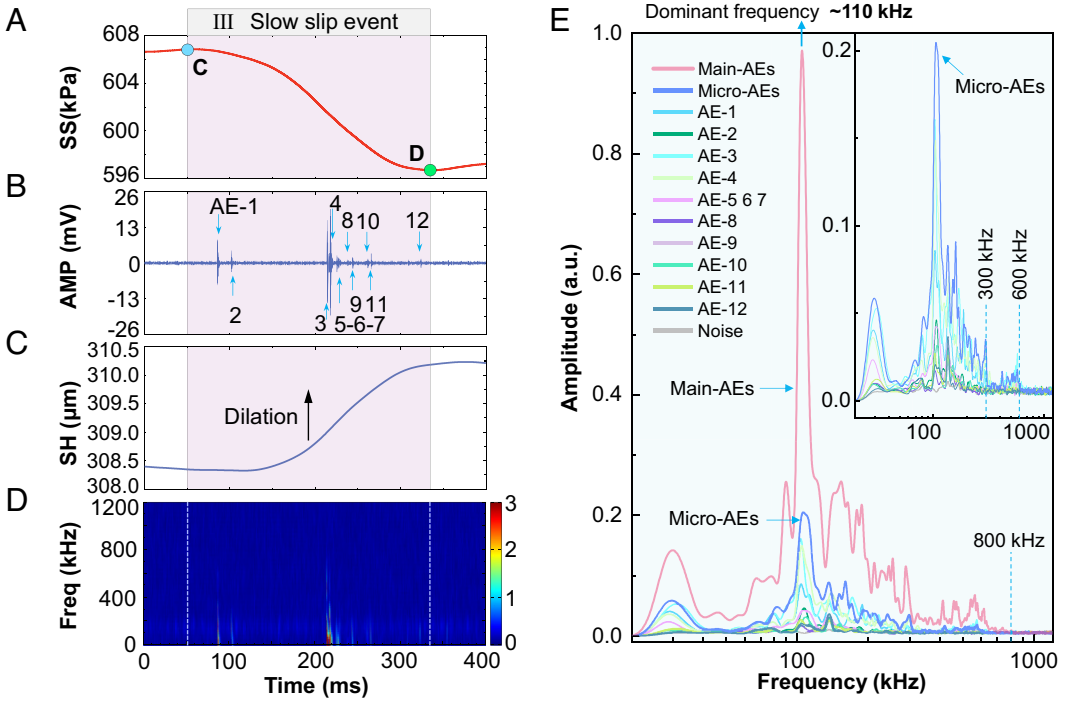

Fig. 3. The selected result of the slow-slip event in Fig. 1*H* depicts the event sequences of SS, AE waveform, SH, and spectrum of AEs in the time domain (400 ms). (*A*) Variations in SS with time in 400 ms (slow slip); the red curve is the SS after smoothing of the raw data. (*B*) During the slow stress drop process, there was a delay between the onset of AEs and the gradual decrease in stress. Intermittent AEs, labeled as AE 1-12, were observed during this period of slow stress drop, amplitude (AMP). (*C*) The sample's thickness dilation is initiated in the stress drop process; the blue curve is the SS after smoothing of the raw data, SH. (*D*) The spectrum of AEs in the time domain, frequency (Freq). (*E*) The marginal spectrum (amplitude vs. frequency) in a specific time window of 8 ms. The main-AEs and micro-AEs were taken from the fast slip event in Fig. 2*B*, and AEs 1-12 were taken from the slow slip event in Fig. 3*B*. The insert shows the enlargement of the signals in the amplitude range of 0 to 0.2.

reaches ~800 kHz. The amplitude of the micro-AEs is smaller; the cutoff frequency reaches ~600 kHz. As shown in the insert of Fig. 3*E*, we zoom into the signals in the amplitude range of 0 to 0.2. The signal amplitude during the slow slip process is smaller than micro-AEs, some cutoff frequencies reach ~600 kHz, and most of them are only below 300 kHz.

Statistical Properties of Fast-Slip and Slow-Slip Events. An advantage of our system was that the ultrahigh sampling rate signals could be used to compare the full-time variation of fast-slip and slow-slip events. In order to better display the statistical results of the two slip events under different normal stresses, we normalized the SS variation rate and slip duration, respectively. We present a collapse of different slip events in which the SS variation rate (dSS/dt) (the slope of SS curves for fast-slip events and slow-slip events), normalized by the maximum SS variation rate of each event (dSS/dt)max, and the slip time t of the fast-slip events and slow-slip events, normalized by the slip duration, are plotted (Fig. 4). These temporal avalanche profiles have a similar pattern under different normal stresses. In the fast-slip event (Fig. 4*A*), there is a significant decrease in stress during the large stress drop process (A-T in Figs. 2*A* and 4*A*). This process rapidly decreases the stress until it reaches a transition point (T point in Figs. 2*A* and 4*A*). After this transition point, there is a minor stress drop process (T-B) characterized by a small rise in stress, followed by a gradual and slight decrease in stress at a slower rate. The stress variation rate reaches a peak between A and T before the midpoint of the slip duration. In the process of slow slip, only one stress drop (C-D in Figs. 3*A* and 4*B*) was observed. The stress variation rate increased first and then decreased, and the stress drop rate reached its peak near the midpoint of slip duration The normalization factors of two axes are calculated by the (dSS/dt)max and the duration of each slip events. In order to find out whether the normalization factors depend on the applied normal stress, we plot the normalization factors vs. normal stress in Fig. 4 *C*–*F*. Linear fitting found that (dSS/dt)max has a strong linear correlation with normal stress (R^2 for fast and slow slip events are 0.98 and 0.99, respectively). The duration is independent of the normal stress.

Fast and slow slip events could be quantitatively distinguished by stress drop and slip duration. The fast-slip events and slow-slip events under different normal stress conditions were statistically analyzed. The scatter plot in double logarithmic coordinates is shown in Fig. 5*A*. The stress drop caused by the fast-slip event in the laboratory earthquake is one order of magnitude higher than that of the slow-slip event. The duration of the fast-slip event is one order of magnitude smaller than that of the slow-slip event. The fast slip duration is about 10 to 20 ms, manifested as a rapid release of elastic strain energy. The duration of the slow slip process fluctuates within 200 to 700 ms, which corresponds to the slow release of stress. In order to explore the relationship between the two types of slip duration and the stress drop under different normal stress conditions, we made a cumulative density function (CDF) for the slip duration and the stress drop of the two types of events. The CDF can be written as Eq. **1**:

$$F(a) = P(x \leq a), \qquad [1]$$

where $F(a)$ is the CDF, and $P(x \leq a)$ is the sum of the probability of all values less than or equal to a. We plotted them on the double logarithmic coordinate diagram (Fig. 5 *B* and *C*). The slip duration has a similar distribution interval under different normal stress conditions, indicating that the duration of the two types of events is independent of the magnitude of the normal stress (in the normal stress range we are investigating). In the process of both fast and slow slip, the magnitude of the stress drop positively correlates with the magnitude of the normal stress.

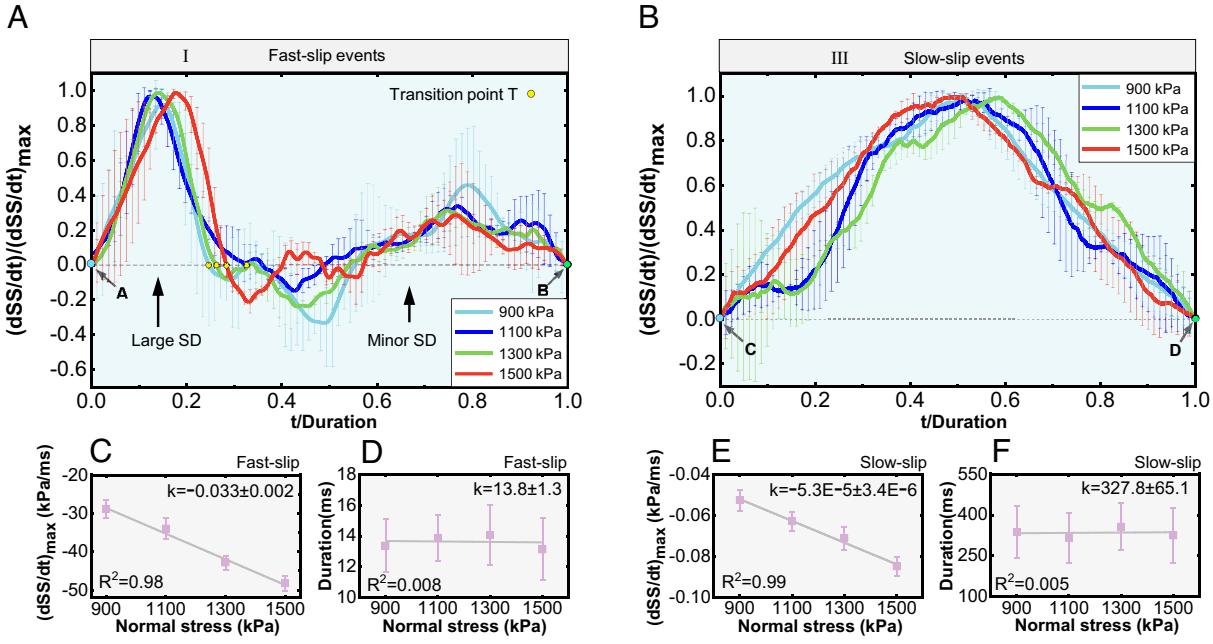

Fig. 4. Temporal avalanche profiles and linear fitting of normalization factors and normal stress of fast-slip and slow-slip events in uniform size tests. (*A*) SS variation rate normalized by the maximum SS variation rate of the fast-slip events at four normal stresses. Profiles are averaged over the whole slip duration. Error bars are calculated as the SEM. Above the dotted line is the stress drop, otherwise the stress rise. Large SD (large stress drop process), minor SD (minor stress drop process). Points A and B represent the start and the cessation of the stress drop in the fast-slip event. The appearance time of the T point in the process of stress drop under different normal stresses is different. (*B*) SS variation rate normalized by the maximum SS variation rate of the slow-slip events at four normal stresses. Profiles are averaged over the whole slip duration. Error bars are calculated as the SEM. Above the dotted line is the stress drop, otherwise the stress rise. Points C and D represent the start and the cessation of the stress drop in the slow-slip event. (*C*) The linear fitting result of the maximum SS variation rate and applied normal stress in fast-slip. (*D*) The linear fitting result of the slip duration and applied normal stress in fast-slip. (*E*) The linear fitting result of the maximum SS variation rate and applied normal stress in slow-slip. (*F*) The linear fitting result of the slip duration and applied normal stress in slow-slip. In the linear fitting, R2 is the coefficient of determination, k is the slope, and error bars are calculated as the SEM.

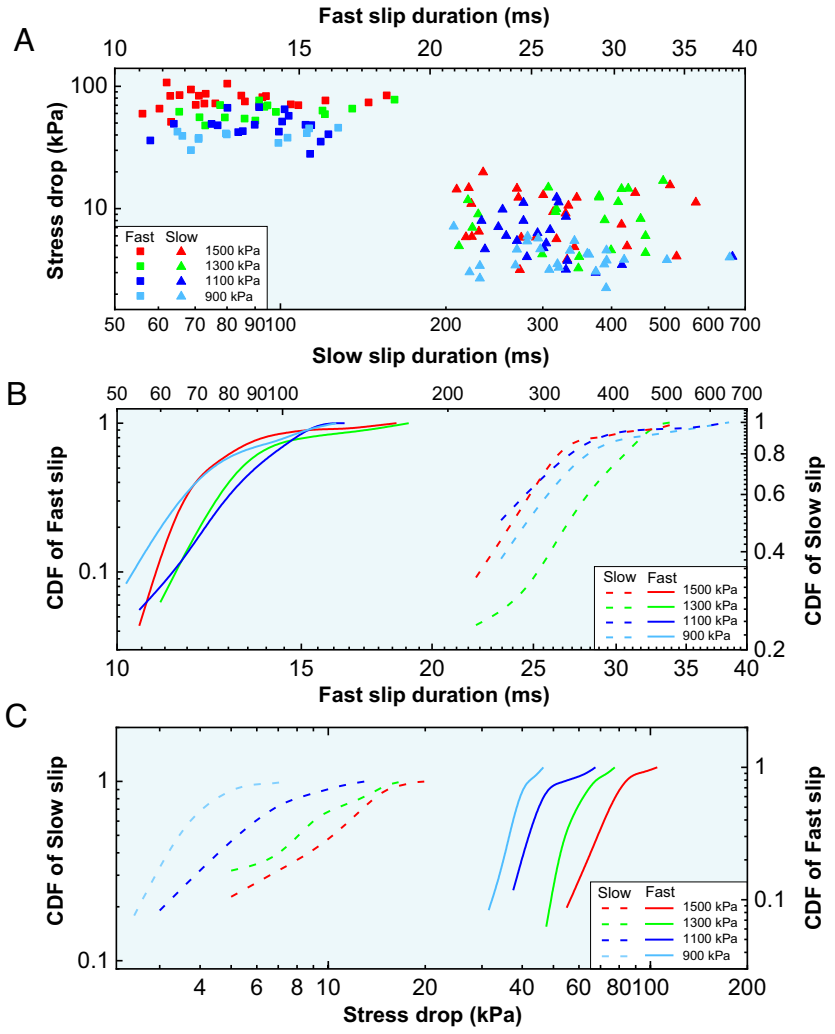

Fig. 5. Stress drop and slip duration of two slip events in uniform size tests. (*A*) Stress drop versus slip duration for fast-slip and slow-slip events. The fast-slip events are shorter in duration than the slow-slip events, and the stress drop of fast-slip events is larger than the slow-slip events. (*B*) The CDF of slip duration in fast-slip events and slow-slip events. The fast-slip events are shorter in duration than the slow-slip events. The slip duration is independent of the magnitude of the normal stress (*C*) The CDF of stress drops in fast-slip events and slow-slip events. The stress drop of fast-slip events is larger than the slow-slip events. The magnitude of the stress drop positively correlates with the magnitude of the normal stress.

We also conducted a set of the large particle size distribution (PSD) (0.2 to 2 mm) glass sphere ring shear tests under 1,500 kPa normal stress (*SI Appendix*, Figs. S6 and S7). Three phases of the stick–slip process were consistent with the uniform size tests (Fig. 1). We analyzed the large PSD glass sphere ring shear synchronous acquisition results of fast-slip events in 18 ms and slow-slip events in 600 ms (*SI Appendix*, Fig. S8) and observed the same characteristics as in the uniform size test.

Discussion

The Transient Dilation during the Fast-Slip. There is still a significant debate over whether the sample thickness is dilated or compacted during fast slip. In recent studies (13, 21–24), the measurements were interpreted in the following manner: During the slip event, the reduction of the SS is accompanied by compaction, whereas in between the slip events, the system recovers by dilation. This is somewhat surprising as this contrasts the classical view which associates slip with dilation in compact samples (25–27, 43). However, Cain et al. argue that the dilation was similar in magnitude to the signal noise level, limiting the conclusions that could be drawn from the measurement (22). We note that recent publications (13, 21–24) have used spring-returned LVDT to record thickness changes during slip and only observed a compaction process. However, the classic view (25) used a separated LVDT (unguided LVDT) with a low sampling rate of 1 kHz. Our observation used an unguided LVDT sensor and increased the sampling rate to 10 MHz. The dynamic response of the spring-returned LVDT (~10 Hz) is much lower than the unguided LVDT (2 kHz). For comparison, we added a spring-returned LVDT in the ring shear apparatus; the sample thickness variation during the fast-slip was synchronously recorded with 10 MHz acquisition rate by using unguided LVDT and spring-returned LVDT (Fig. 6). Before the stress drop, the system recovers by dilation. The transient dilation process during the fast-slip recorded by unguided LVDT is associated with stress reduction; then, we observed the compaction takes place (Fig. 6 *A* and *B*). The transient dilation process during the fast-slip was not observed by using spring-returned LVDT. We only observed a compaction process associated with stress reduction, which lasted longer than the stress reduction (Fig. 6*C*). The transient dilation process was also not observed by using the spring-returned LVDT in recent studies (21–24), and these studies observed that compaction was associated with the slip. In fact, in our observation and recent

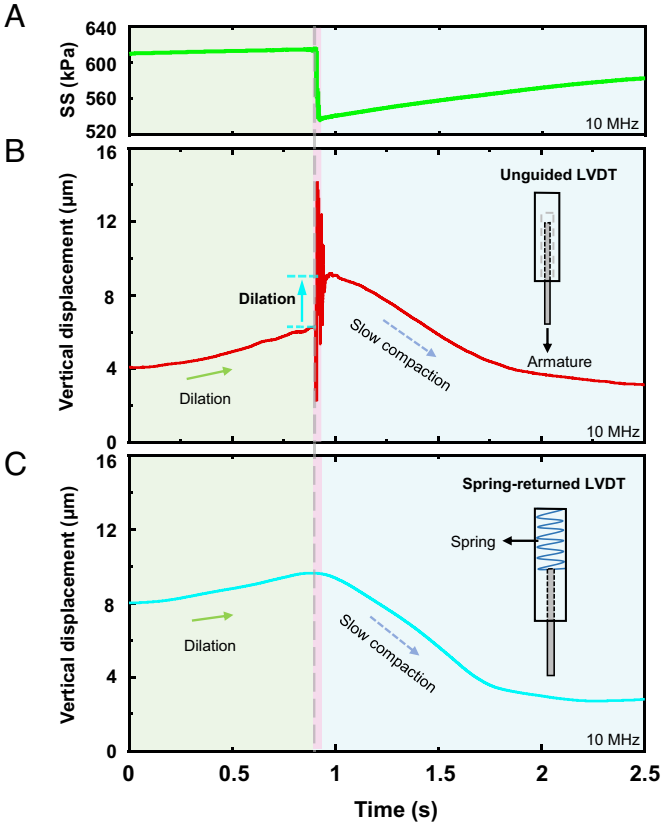

Fig. 6. The unguided LVDT recorded more detailed layer thickness variation information than the spring-returned LVDT. (*A*) Stress drop during the fast-slip. SS. The light red area marks the slip process. (*B*) In the case of unguided LVDT, instantaneous dilation during the stress drop was recorded (red block), while the slow compaction occurred after the stress drop. (*C*) In the case of spring-returned LVDT, the instantaneous dilation during the stress drop was not recorded; only slow compaction was observed.

studies, the compaction events observed by using the spring-returned LVDT were associated with stress reduction. However, our observation of compaction lasted longer than the stress reduction; we think that this compaction may be a phenomenon, which is in agreement with that observed in the field (28–30): Fault compaction occurs after the earthquake.

The use of the unguided LVDT is the root cause of observing the transient dilation. This study provides more insight into unresolved puzzles about sample compaction or dilation during slip. The results of this study indicate that the sample is in dilation during slip, followed by compaction. This phenomenon is consistent with what is observed in the field: the fault zone experiences dilation during the slip event and compaction after the earthquake (28–30).

The AE Characteristics of Free-Drop Collision Test. We conducted free-drop collision tests with different drop-off heights to explore the AE spectrum and waveform characteristics during the collision process (Fig. 7 *A* and *B*); see *SI Appendix* for the full discussion. As shown in Fig. 7*B*, the AE waveform of the free-drop collision test (drop-off height 40 mm) is characterized by a clear AE burst, and the cutoff frequency reaches ~650 KHz. The cutoff frequency and amplitude of the AE burst generated by the collision at different drop-off heights (5, 10, 20, 30, 40, and 90 mm) are positively correlated with the collision velocity (*SI Appendix*, Fig. S9). We compared the power spectrum of different free-drop collision tests quantitatively by plotting the marginal spectrum in a specific time window of 8 ms (Fig. 7*C*). As the drop-off height increases, the amplitude and cutoff frequency are increasing. The dominant frequency of these AE signals is about 110 kHz, which is consistent with the AE signals during the fast and slow slip events (Fig. 3*E*). The observed AEs during fast and slow slip show similar AE characteristics with the free-drop test. Thus, we can semiquantitatively judge the collision intensity inside the granular assembly according to the cutoff frequency and amplitude of the AE burst. As shown in Fig. 3*E*, the main-AEs in the fast slip reach about 800 kHz for intense collision, and the micro-AEs in the fast slip reach about 600 kHz for weak collision. Some AEs in the slow slip reach about 600 kHz, and most of the other AEs are below 300 kHz, indicating that these intermittent collisions have different intensities.

The Mechanism of the Fast-Slip Event. Spatial heterogeneity of contact forces between grains varies during the shear process. As the SS is applied, the force chain network exhibits an anisotropic nature (34). The force chain network structures can be classified into three groups based on the magnitude of the contact force between the grains (35–38): a strong force chain network that carries stress balancing paths, a weak force chain network that bears less stress, and a loose granular structure are least stressed. The strong force chain collapse induces the intense grain collision, and the weak force chain collapse induces the weak grain collision. As shown in Fig. 3*E*, the largest amplitude AE is the main-AEs in the fast slip; thus, we speculated that the strong force chain collapse is responsible for the fast slip.

In the stick phase (Fig. 1*B*), the strong force chains accumulate elastic strain energy with the shearing process (35, 37). We observed that the onset of main-AEs preceded the fast stress drop (Fig. 2 *A* and *B*); thus, we speculate that there are some local grains that slip prior to overall force chain failure and may trigger the fast slip process. There are mainly two stages during the fast slip process: short compaction and dilation–vibration (Figs. 2*C* and 6*B*). We make a hypothesis of physical mechanism about the short compaction and dilation–vibration.

Compaction or dilation is dependent on the packing state of the sample (44, 45). Before the fast slip, the sample is comparatively loose due to the dilation (Fig. 6 *B* and *C*). In stage one, once the SS of one or two strong force chains exceeds the shear strength of the contact grains, the strong force chains fail (32, 33), which leads to elastic strain energy rapidly releasing (the large stress drop A-T in Fig. 2*A*). The grains with high kinetic energy impact the surrounding grains, exciting a large-amplitude AE (main-AEs in Fig. 2*B*) with high-frequency bandwidth (39) (Fig. 2*D*). The collision between grains presents a mechanical impulse imparted on the granular structure, which precipitates a cascade of chain failures of the force chain network (32, 39). The chain failures lead to granular assembly collapses, so a short compaction pulse was observed during the rapid release of stress (Figs. 2*C* and 6*B*).

In stage two (Figs. 2*C* and 6*B*), after a short compaction, the granular system became dense. After the grain collision caused by the force chain collapse, the grains continue to slide and cause dilation of the sample. Meanwhile, the strong grain collisions cause the vibration of the granular sample.

We also observed the approximate synchronous vibrations of SS and sample thickness (Fig. 2 *A* and *C*) during the minor stress drop process (T-B in Fig. 2*A*); we think that the mechanical impulse caused by grain collisions continues to vibrate the granular assemblies, resulting in the approximate synchronous vibrations of the SS and the sample thickness. Upon the cessation of the layer vibration (Figs. 1*G*, 2*C*, and 6*B*), the grains recontact to accumulate elastic strain energy and adjust the structure of granular assemblies, resulting in slow compaction of layer thickness (Figs. 1*G*, 2*C*, and 6*B*) and rearrangement of the force chain network structures.

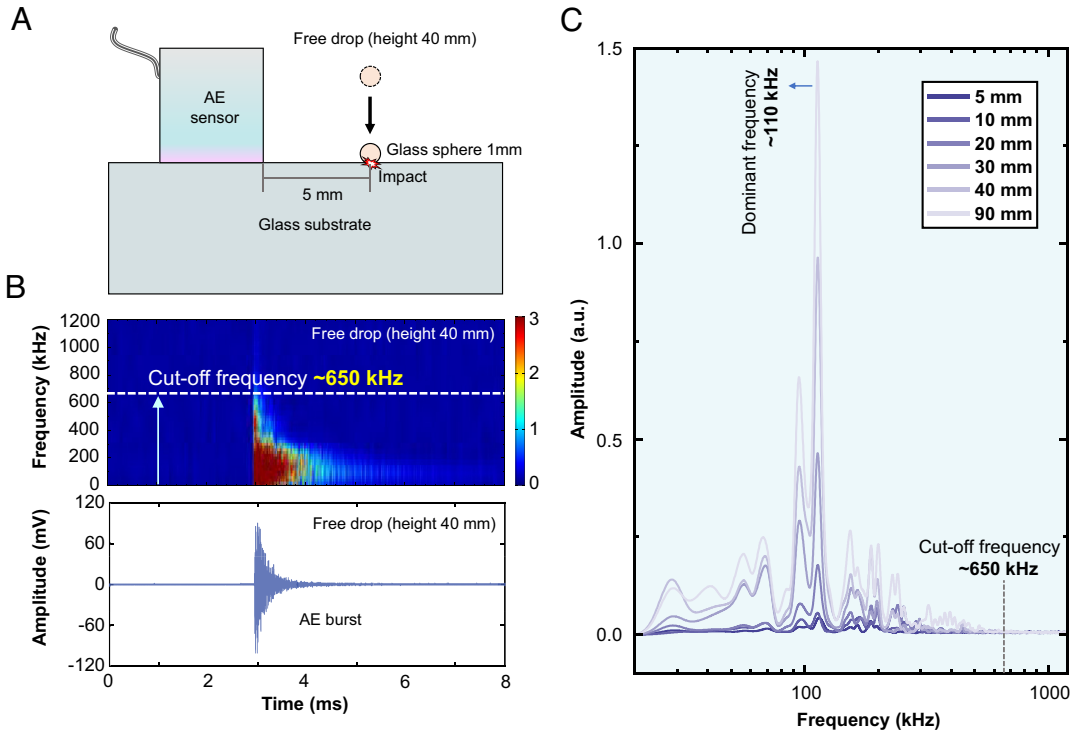

Fig. 7. Device drawing and experimental results of free drop collision test. (*A*) Free drop collision test with 1-mm glass sphere, drop-off height 40 mm. (*B*) The AE spectrum and waveform of the collision test. (*C*) The marginal spectrum of all the free drop collision tests with different drop-off heights in a specific time window of 8 ms.

The Mechanism of Slow-Slip Event. The fast earthquakes are responsible for catastrophic ground vibration, but the slow earthquake may last for several months and will not cause catastrophic ground vibration (6–8). The AE signal with clear burst suggests collision of the grains (39, 40, 42). As shown in Fig. 3, during the slow slip, the small-amplitude AE signal is intermittent with clear burst, and the grain collision intensity is much weaker than that of the fast slip. The weak force chain collapse induces the weak grain collision. Thus, we speculated that the weak force chain collapse is responsible for the slow slip. Both fast and slow slips in granular assemblies exhibit dilatancy, which may be caused by the collapse of strong force chains in the former and weak force chains in the latter. Despite the differences in force chain strength, the physical processes involved in fast and slow slips are similar. During the slow stress drop, only dilation was observed (Fig. 3*C*). Moreover, in the triaxial compression experiments, it is also observed that the slow decrease of SS is accompanied by the slow volume dilation. During constant speed loading, the shear input power (rate of shear input work) is constant, and this energy is converted into plastic dilation deformation, which reduces the SS to maintain conservation of energy (Cam-clay model) (46). Using X-ray computed tomography (CT) under triaxial compression, it was observed that the rearrangement of the force chain networks leads to the slow release of SS, and the grains rolling across the surrounding grains cause volume dilation (47).

Before the slow slip occurs, the thickness of the sample is relatively small (Fig. 1*D*), and the granular assembly is dense. When weak force chains fail and a slow slip occurs, the close-packed grains must seek new positions to accommodate the slip, leading to dilation in the thickness of the sample (Fig. 3*C*). The delay in the initiation of sample thickness dilation observed during the slow-slip event (Fig. 3 *A* and *C*) suggests that the release of elastic strain energy in the weak force chain occurs before the conversion from shear input work to plastic dilation deformation begins. After the adjustment of the grains structure of the weak force chain, the bearing stress of the weak force chain reduced to lower level (slow stress drop in Fig. 3*A*). The grain collisions are very weak during the slow slip (Fig. 3*E*), and the mechanical impulse could not be excited to perturb the failure of strong chain; therefore, the failure of weak force chain will not lead to the overall failure of the granular assemblies.

It was observed that the granular packings dilated slowly during the stick process (Fig. 6 *B* and *C*) (13, 21–24). This suggests that initially, force chains form and strengthen, and then the packings start to creep, leading to dilation (22). Once the dilation reaches an almost similar height, the fast-slip events begin (21–24). Conceptually, this transition from stick to slip will therefore be functions of the granular layer thickness. We observe that slow slips with dilation accelerate the dilation progress during stick; therefore, the rearrangement of weak force chain during slow slips is more likely to lead to the fast slip.

Implications for Fast and Slow Earthquake Slip Models. Coseismic strain tensors and postseismic analysis have confirmed that fault zones undergo dilation during coseismic slip and subsequently through compaction after the earthquake (28–30). In our synchronous ultrahigh speed acquisition stick–slip experiment, we found the similar variation process of the granular fault thickness as that of field earthquake. The granular assemblies dilated during the fast slip process, and even the vibration of the SS and SH was recorded. After the fast slip, the slow compaction (hundreds of milliseconds) was observed. Moreover, different from only coseismic dilation in the field, a very fast (~2 ms) compaction at the beginning of the fast slip in our experiment was observed (Fig. 2*C*). Although the glass spheres used in our experiment are simplified compared to real fault gouge, they are all granular materials and have the similar potential stick–slip mechanism (48). The results of this laboratory experiment are consistent with the field seismic observation, which shows that our observations have implications for the mechanism of real earthquakes.

It was reported that slow earthquakes may play roles in stress transfer and stress redistribution in faults, thus triggering fast earthquakes (8–11). Fast and slow slip modes may occur in the same fault, which indicates that the occurrence of fast and slow earthquakes has more complex mechanism (1). Our experimental observations reveal that the fast and slow slip modes would occur in the same granular assemblies without changing the external loading conditions (16, 17). The sample thickness dilated during slow-slip events, which accelerated the dilation of stick progress. Therefore, the force chain structure after slow slips is more likely to trigger fast slip; this is consistent with field observations (8–11).

The synchronous high-resolution time sequences from the experiments allow us to understand the mechanism that fast-slip and slow-slip events are different slip instability modes for the same granular fault. Our observations, on the same glass sphere assemblies, indicate fast and slow slip modes that are controlled by the failure modes of strong and weak force chains, respectively. We believe that the deformation and failure of strong and weak force chains also controls the slip mechanism of fast and slow earthquakes in the field.

Our experiment is a physical mechanical model of seismic mechanism; we also understand that it takes a long time to establish a bridge between physical model and natural setting through physical experiments. This study provides important insights on the slip mechanisms that fast and slow earthquakes would occur in the same granular fault, and the effect of structure rearrangement and stress redistribution in faults must be taken into account when formulating models for fast earthquake prediction. Furthermore, we believe that it is necessary to visually observe the force chain structural variation of the granular assemblies in the process of high-resolution synchronous acquisition. It will further provide the physical mechanism of fast and slow slip failure in granular materials and then provide significant insights to fast and slow earthquake slip models.

Materials and Methods

Experimental Apparatus. We performed our experiments using a servo-controlled ring shear apparatus (Fig. 8 and *SI Appendix*, Fig. S10*A*), which provided a constant shear rate without displacement restriction under different chosen normal stresses. The servo system continuously feedback-controlled the normal stress applied by a hydraulic loading unit via the force sensor. The servo motor provided a constant shear angular speed (1.5°/min) to drive a shear box rotating at an average tangential speed of 1 mm/min. The upper and lower platens were fixed with teeth to ensure shearing between glass spheres rather than sliding against the platens.

The SH was measured by the unguided LVDT (D5/40WRA, noncontact operation, accuracy ±0.1 μm, operating frequency is consistent with the target, RDP Electronics Ltd, UK) and the spring-returned LVDT (GHNV19R, contact operation, accuracy ±0.1 μm, operating frequency is 10 Hz, ABEK Ltd, CHN). The unguided LVDT transducer and armature were securely held in two brackets. These brackets were fixed to the upper plate of the servo-hydraulic unit and the substrate, respectively (Fig. 8 and *SI Appendix*, Fig. S10*B*). This setup guarantees that the armature moves along with the target, and ensures the response frequency of the sensor matches the frequency of the target motion. Therefore, the transient and subtle changes in the thickness of glass sphere assemblies could be recorded (Fig. 6*B*). In the case of the spring-returned LVDT, the dynamic response of the sensor depends on the response frequency of the spring, which is much lower than the dynamic response of unguided LVDT (*SI Appendix*, Fig. S10*B*). The output voltages from the unguided LVDT were digitized by the amplifier (S7AC, bandwidth 2 kHz, RDP Electronics Ltd, UK). The AE sensor (WD, φ18 mm × 17 mm, peak frequency 1,000 kHz, peak sensitivity 55 dB, Physical Acoustics Corporation, USA) was fixed on the side of the upper platen (Fig. 8) and remained in the same position to ensure a fair time–frequency comparison of the experiments. The AE signal was bandpass filtered by a preamplifier (2/4/6C, Physical Acoustics Corporation, USA) at 20 to 1,200 kHz with 20 dB sensitivity. The SS signal from the torque sensor, the SH signal from LVDT, and the AE signal were recorded simultaneously at a 10-MHz sampling rate (*SI Appendix*, Fig. S10*C*) via a multiple isolated channel ultrahigh speed acquisition system (NI CompactDQA, PXIe-1084 & BNC-2110, National Instrument Company, USA).

As schematically shown in *SI Appendix*, Fig. S11*A*, the annular sample cavity is detachable. The annular sample cavity was installed before loading (*SI Appendix*, Fig. S11*B*). A cutaway diagram of the annular sample cavity is shown in *SI Appendix*, Fig. S11*C*. The annular sample cavity was made of stainless steel and had an inner diameter of 50 mm and an outer diameter of 100 mm; the height of the upper and the lower part of the cavity was 15 mm and 10 mm, respectively. A Teflon ring was installed on the contact surface between the outer ring and the shear box to reduce friction. This design allowed the shear to occur in a horizontal shear zone around a stress localization shear plane caused by the relative rotation of the upper and lower sample cavities.

To make sure that the spectral response of the AE sensor under our data acquisition set up does not influence of the overall results and interpretations, we conducted a quick sensor calibration as detailed in *SI Appendix*, Figs. S12 and S13.

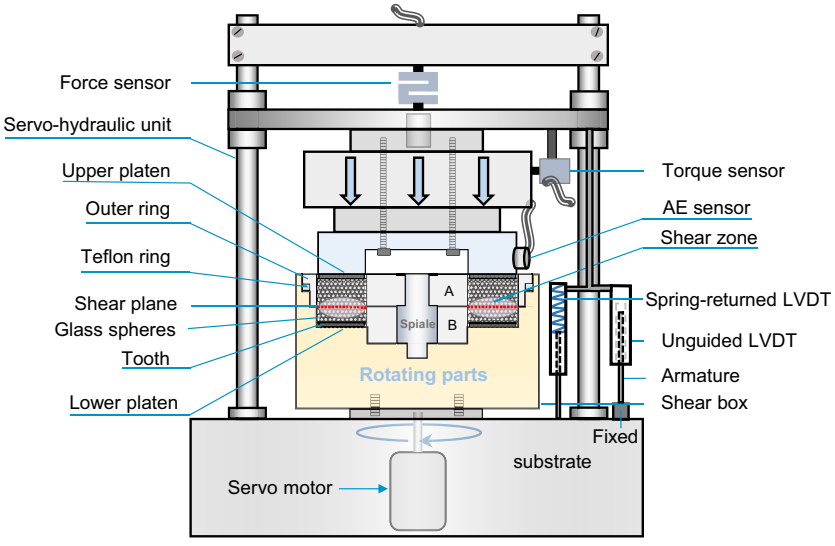

Fig. 8. The ring shear configuration. Cross-section schematic diagram of the ring shear apparatus. The vertical servo-hydraulic unit applies controlled normal stress, and the servo motor drives shear at a constant angular velocity. LVDT = linear variable differential transformer.

Sample Preparation. Glass spheres have reproducible stick–slip properties and are widely used as a laboratory analog of fault gouge. This material also allows us to control variables such as grain shape and PSD. The initial sample density of the glass sphere packings with a uniform size (0.8 to 1 mm) in the annular sample cavity with 25 mm height and width was approximately 1,500 kg/m^3. An inspection of glass spheres after experiments found no grain crushing. The glass spheres were ultrasonically cleaned for 30 min and then dried in an oven at 100 °C for 24 h before we experimented at room temperature and controlled humidity.

Data, Materials, and Software Availability. All study data are included in the article and/or *SI Appendix*.

ACKNOWLEDGMENTS. We are supported by the NSF for Distinguished Young Scholars of China (42325703) and the National Basic Research Program of China: basic research fund (42090051).

Author affiliations: [a]State Key Laboratory of Geo-Hazard Prevention and Geo-Environment Protection, Chengdu University of Technology, Chengdu 610059, China; [b]Department of Civil and Environmental Engineering, The Hong Kong Polytechnic University, Hong Kong Special Administrative Region 100872, China; [c]Institute of Geological and Nuclear Sciences, Lower Hutt 9040, New Zealand; [d]Department of Civil and Environmental Engineering, University of Massachusetts, Amherst, MA 01003; [e]Institut Langevin, École supérieure de physique et de chimie industrielles de la Ville de Paris (ESPCI) Paris, Université Paris Sciences & Lettres (PSL), CNRS, Paris 7587, France; and [f]School of Physics and Astronomy, Shanghai Jiaotong University, Shanghai 200240, China

1. D. M. Veedu, S. Barbot, The Parkfield tremors reveal slow and fast ruptures on the same asperity. *Nature* **532**, 361–365 (2016).
2. W. F. Brace, J. D. Byerlee, Stick–slip as a mechanism for earthquakes. *Science* **153**, 990–992 (1966).
3. C. Voisin, J.-R. Grasso, E. Larose, F. Renard, Evolution of seismic signals and slip patterns along subduction zones: Insights from a friction lab scale experiment. *Geophys. Res. Lett.* **35**, 1–5 (2008).
4. A. T. Linde, M. T. Gladwin, M. Johnston, R. L. Gwyther, R. G. Bilham, A slow earthquake sequence on the San Andreas fault. *Nature* **383**, 65–68 (1996).
5. S. Y. Schwartz, J. M. Rokosky, Slow slip events and seismic tremor at circum-Pacific subduction zones. *Rev. Geophys.* **45**, 1–32 (2007).
6. D. R. Shelly, G. C. Beroza, S. Ide, Non-volcanic tremor and low-frequency earthquake swarms. *Nature* **446**, 305–307 (2007).
7. S. Ruiz *et al.*, Intense foreshocks and a slow slip event preceded the 2014 Iquique Mw 8.1 earthquake. *Science* **345**, 1165–1169 (2014).
8. E. Araki *et al.*, Recurring and triggered slow-slip events near the trench at the Nankai Trough subduction megathrust. *Science* **356**, 1157–1160 (2017).
9. A. Kato *et al.*, Propagation of slow slip leading up to the 2011 Mw 9.0 Tohoku-Oki earthquake. *Science* **335**, 705–708 (2012).
10. Y. Ito *et al.*, Episodic slow slip events in the Japan subduction zone before the 2011 Tohoku-Oki earthquake. *Tectonophysics* **600**, 14–26 (2013).
11. L. Wallace *et al.*, Large-scale dynamic triggering of shallow slow slip enhanced by overlying sedimentary wedge. *Nat. Geosci.* **10**, 765–770 (2017).
12. T. Baumberger, F. Heslot, B. Perrin, Crossover from creep to inertial motion in friction dynamics. *Nature* **367**, 544–546 (1994).
13. P. A. Johnson *et al.*, Nonlinear dynamical triggering of slow slip on simulated earthquake faults with implications to Earth. *J. Geophys. Res. Solid Earth* **117**, 1–9 (2012).
14. B. M. Kaproth, C. Marone, Slow earthquakes, preseismic velocity changes, and the origin of slow frictional stick–slip. *Science* **341**, 1229–1232 (2013).
15. D. Cui *et al.*, Stick–slip behaviours of dry glass beads in triaxial compression. *Granul. Matter* **19**, 1–18 (2017).
16. J. R. Leeman, D. M. Saffer, M. M. Scuderi, C. Marone, Laboratory observations of slow earthquakes and the spectrum of tectonic fault slip modes. *Nat. Commun.* **7**, 1–6 (2016).
17. J. R. Leeman, C. Marone, D. M. Saffer, Frictional mechanics of slow earthquakes. *J. Geophys. Res. Solid Earth* **123**, 7931–7949 (2018).
18. J. C. Gu, J. R. Rice, A. L. Ruina, S. T. Tse, Slip motion and stability of a single degree of freedom elastic system with rate and state dependent friction. *J. Mech. Phys. Solids* **32**, 167–196 (1984).
19. Y. Liu, J. R. Rice, Spontaneous and triggered aseismic deformation transients in a subduction fault model. *J. Geophys. Res. Solid Earth* **112**, B09404 (2007).
20. S. Ide, G. C. Beroza, D. R. Shelly, T. Uchide, A scaling law for slow earthquakes. *Nature* **447**, 76–79 (2007).
21. Y. Jiang, G. Wang, T. Kamai, Acoustic emission signature of mechanical failure: Insights from ring shear friction experiments on granular materials. *Geophys. Res. Lett.* **44**, 2782–2791 (2017).
22. R. G. Cain, N. W. Page, S. Biggs, Microscopic and macroscopic aspects of stick–slip motion in granular shear. *Phys. Rev. E* **64**, 016413 (2001).
23. M. M. Scuderi, B. M. Carpenter, C. Marone, Physicochemical processes of frictional healing: Effects of water on stick–slip stress drop and friction of granular fault gouge. *J. Geophys. Res. Solid Earth* **119**, 4090–4105 (2014).
24. C. Hulbert *et al.*, Similarity of fast and slow earthquakes illuminated by machine learning. *Nat. Geosci.* **12**, 69–74 (2019).
25. S. Nasuno, A. Kudrolli, A. Bak, J. P. Gollub, Time-resolved studies of stick–slip friction in sheared granular layers. *Phys. Rev. E* **58**, 2161–2171 (1998).
26. P. A. Thompson, G. S. Grest, Granular flow: Friction and the dilatancy transition. *Phys. Rev. Lett.* **67**, 1751–1754 (1991).
27. Y. Zhang, C. S. Campbell, The interface between fluid-like and solid-like behaviour in two-dimensional granular flows. *J. Fluid Mech.* **237**, 541–568 (1992).
28. W. D. Barnhart, R. D. Gold, J. Hollingsworth, Localized fault-zone dilatancy and surface inelasticity of the 2019 Ridgecrest earthquakes. *Nat. Geosci.* **13**, 699–704 (2020).
29. C. H. Scholz, Post-earthquake dilatancy recovery. *Geology* **2**, 551–554 (1974).
30. E. J. Fielding, P. R. Lundgren, R. Bürgmann, G. J. Funning, Shallow fault-zone dilatancy recovery after the 2003 Bam earthquake in Iran. *Nature* **458**, 64–68 (2009).
31. K. Mair, K. M. Frye, C. Marone, Influence of grain characteristics on the friction of granular shear zones. *J. Geophys. Res. Solid Earth* **107**, ECV 4–1–ECV 4–9 (2002).
32. J. L. Anthony, C. Marone, Influence of particle characteristics on granular friction. *J. Geophys. Res. Solid Earth* **110**, 1–14 (2005).
33. A. Tordesillas, Force chain buckling, unjamming transitions and shear banding in dense granular assemblies. *Philos. Mag.* **87**, 4987–5016 (2007).
34. L. Zhang, Y. J. Wang, J. Zhang, Force-chain distributions in granular systems. *Phys. Rev. E* **89**, 012203 (2014).
35. M. E. Cates, J. P. Wittmer, J. P. Bouchaud, P. Claudin, Jamming, force chains, and fragile matter. *Phys. Rev. Lett.* **81**, 1841–1844 (1998).
36. F. Radjai, D. E. Wolf, M. Jean, J.-J. Moreau, Bimodal character of stress transmission in granular packings. *Phys. Rev. Lett.* **80**, 61–64 (1998).
37. L. Staron, F. Radjai, Friction versus texture at the approach of a granular avalanche. *Phys. Rev. E* **72**, 041308 (2005).
38. P. P. Jose, I. Andricioaei, Similarities between protein folding and granular jamming. *Nat. Commun.* **3**, 1–8 (2012).
39. G. Michlmayr, D. Cohen, Mechanisms for acoustic emissions generation during granular shearing. *Granul. Matter* **16**, 627–640 (2014).
40. G. Michlmayr, D. Cohen, D. Or, Sources and characteristics of acoustic emissions from mechanically stressed geologic granular media–A review. *Earth Sci. Rev.* **112**, 97–114 (2012).
41. P. A. Johnson *et al.*, Acoustic emission and microslip precursors to stick–slip failure in sheared granular material. *Geophys. Res. Lett.* **40**, 5627–5631 (2013).
42. W. L. Lin, A. Liu, W. W. Mao, Use of acoustic emission to evaluate the micro-mechanical behavior of sands in single particle compression tests. *Ultrasonics* **99**, 105962 (2019).
43. A. D. Berman, W. A. Ducker, J. N. Israelachvili, Origin and characterization of different stick—slip friction mechanisms. *Langmuir* **12**, 4559–4563 (1996).
44. C. Marone, C. H. Scholz, Particle-size distribution and microstructures within simulated fault gouge. *J. Struct. Geol.* **11**, 799–814 (1989).
45. C. A. Morrow, J. D. Byerlee, Experimental studies of compaction and dilatancy during frictional sliding on faults containing gouge. *J. Struct. Geol.* **11**, 815–825 (1989).
46. K. H. Roscoe, A. N. Schofield, A. Thurairajah, Yielding of clays in states wetter than critical. *Géotechnique* **13**, 211–240 (1963).
47. Y. Wang, J. M. Que, C. Wang, C. H. Li, Three-dimensional observations of meso-structural changes in bimsoil using X-ray computed tomography (CT) under triaxial compression. *Constr. Build Mater.* **190**, 773–786 (2018).
48. J. A. Åström, H. J. Herrmann, J. Timonen, Granular packings and fault zones. *Phys. Rev. Lett.* **84**, 638–641 (2000).